Hydrodynamic Performance of Deformable Fish Fins and Flapping Foils

M. Bozkurttas[*], H. Dong.[†], R. Mittal[‡]
Department of Mechanical & Aerospace Engineering,
*The George Washington University,*
Washington, DC 20052

P. Madden[§] and G.V. Lauder [**]
Museum of Comparative Zoology
Harvard University,
Cambridge, Massachusetts, USA

A computational study of fish fin hydrodynamics is being conducted concurrently with experimental analysis. The presence of a complex shaped moving boundary makes this a difficult proposition for computational fluid dynamics and here we use a Cartesian grid based immersed boundary solver designed to handle such flows in all their complexity. High resolution, high speed video of fish fin movement during steady swimming by a bluegill sunfish (*Lepomis macrochirus*) is obtained and these are used as a basis for developing a high fidelity geometrical model of the flapping fish fin. Simulations are carried out in order to examine the hydrodynamic performance of the fish fin and understand the wake topology of such fins. The fin motion is highly complex and a number of different strategies including proper orthogonal decomposition of the fin kinematics are used to examine the various kinematical features of the fin motion as well as their impact on the fin performance.

I.   Introduction

THIS work is a part of a research program designed to develop a maneuvering propulsor for AUV's (Autonomous Underwater Vehicle) based on the mechanical design and performance of fish fins. Fishes are notable for their ability to maneuver and to accurately position themselves even in highly unsteady flows. Fish can maneuver in tight spaces and accelerate and decelerate quickly from rest or low speed with the same propulsion system. Also, fish fins are remarkable fluid control devices with supporting bony elements that are under active muscular control. In addition to muscular actuation at the base of the fin which governs overall fin position, fish fins possess a bilaminar design that allows active control of propulsor surface curvature. Fish fins can thus actively resist hydrodynamic bending forces during propulsion and maneuvering. This current ongoing effort is specifically focused on understanding the fluid and structural dynamics of the pectoral fin of the bluegill sunfish that has been studied experimentally in detail by Drucker and Lauder[1]. For a general specimen, the Reynolds number based on fish body length ($L \sim 20$
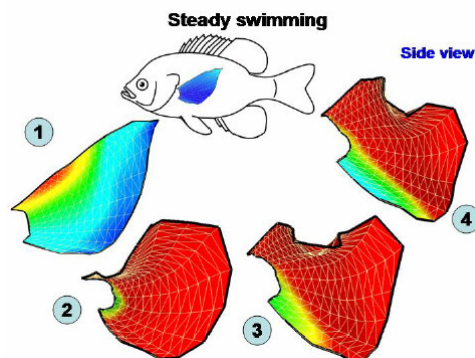
Figure 1. Conformations of the sunfish pectoral fin at four times during the fin beat in steady forward locomotion.
Color reflects the distance from the body, with blue indicating position near the body, and the red positions away from the body.

---

[*] Graduate Student, AIAA Student Member

[†] Research Scientist, AIAA Member

[‡] Associate Professor, Senior AIAA Member

[§] Research Scientist

[**] Professor

cm) and velocity (0.1 to 0.2 ms^{-1}) is about 2x10^4. At this Reynolds number, the attached flow over the body is most likely laminar but is expected to transition rapidly to turbulence in regions of flow separation which might occur downstream of appendages. The flow over the fins can be characterized in terms of a Stokes frequency parameter ($S = \omega A l / \upsilon$) where ω, A and l are the fin angular frequency, amplitude and length respectively and υ is the kinematic viscosity . Typical fin beat frequency of about 2 Hz and fin amplitude and size of about 3cm and 4cm, respectively, gives $S \approx 1.6 \times 10^4$ that is again in the range where laminar attached flow would quickly transition to turbulence post separation. The fins of this fish are also highly flexible, have complex planforms and undergo complicated motions.

Figure 2. 2D deformable flapping foils with limited degrees of freedom (DOF).
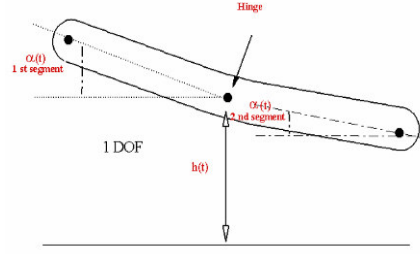*Each foil is made up of a small number of rigid segments linked with hinges.*

In the current study, a DNS/LES immersed boundary solver has been used which is capable of simulating these flows in all their complexity. In particular, the solver is time-accurate and non-dissipative, and allows body motion as well as fluid structure interaction. The details of the solver can be found elsewhere[2]. This solver can also handle highly deformable membranous structures like fish fins which will be discussed in detail here.

Figure 1 shows a pectoral fin motion. The fin position through time is digitized using high speed, high-resolution video from two orthogonal cameras (250 fps, 1024x1024 pixels). Twenty equally spaced frames from the video are selected over each fin beat. Points are digitized along each of the 14 fin rays (the bony elements that support the fin membrane) in the two stereo views to give up to 300 points per frame describing the fin surface in three dimensions. Pectoral fin motion in three dimensions (Fig. 1) is very complex and involves (1) simultaneous movement of the upper and lower edges away from the body, forming two simultaneous leading edges, (2) strong cupping of the fin as it moves away from the body, (3) a wave of bending that moves spanwise along the upper edge of the fin at higher than freestream flow velocity, (4) "dimpling" of the upper fin surface behind the leading edge. On the one hand we would like to understand the fluid dynamics of the realistic fin, and on the other, we would like to extract the essential minimal features of the fin motion that can be incorporated into the engineered fin. A method for extracting these essential features is needed and here we resort to a Proper Orthogonal Decomposition (POD) of the fin kinematics. A complimentary approach of arriving at a simple yet effective "gait" in an engineered deformable fin is also being used. Here we start with a 2D flapping foil with a limited degree of deformation (see Fig. 2) and examine what type of active deformation can improve performance over a comparable rigid foil. Rigid flapping foils have been investigated theoretically (Lighthill, 1970; Chopra, 1976), experimentally (Koochesfhani[3], 1989; Anderson[4], 1996), as well as numerically (Mittal[5], 2003). On the other hand, the observed kinematics of the bluegill's pectoral fin suggests a study of a flapping foil with large-scale active deformation. It should be pointed out that all the work that has been done so far on the flexible flapping foils has focused on *passive* deformation (Katz[6], 1978 & 1979, Prempraneerach et al.[7], 2003). A notable exception is the work (Ramamurti et al.[8], 2002) of a pectoral fin of a Wrasse. Here we describe our efforts in examining the fluid dynamics and thrust performance of an actively deformed flapping foil.

II.   Numerical Methodology

A finite-difference based immersed boundary methodology is used in the current simulations. The key feature of this method is that simulations with complex boundaries can be carried out on stationary non-body conformal Cartesian grids and this eliminates the need for complicated remeshing algorithms that are usually employed with conventional Lagrangian body-conformal methods. In LES, the flow variables are decomposed into a large-scale (or resolved) component, denoted by overbar, and a sub-grid scale component by applying a filtering operation. The filtered Navier-Stokes equations of an incompressible fluid for the resolved field are written in tensor form as:

$$\frac{\partial \overline{u}_i}{\partial x_i} = 0$$

$$\frac{\partial \overline{u}_i}{\partial t} + \frac{\partial \overline{u}_i \overline{u}_j}{\partial x_j} = -\frac{\partial \overline{p}}{\partial x_i} - \frac{\partial \tau_{ij}}{\partial x_i} + \frac{1}{\mathrm{Re}} \frac{\partial^2 \overline{u}_i}{\partial x_j \partial x_j}$$

(1)

where i and j = 1, 2 and 3 correspond to x, y and z coordinates, respectively; and Re is the Reynolds number. In the above equations, $\bar{u}_i$ is the instantaneous filtered velocity component in the i direction, $\bar{p}$ represents the filtered pressure, and t is the non-dimensional time. The equations have been non-dimensionalized by appropriate velocity and length scales. Equation (1) describes the transport of the filtered velocity field and contains the contribution of the subgrid scale (SGS) Reynolds stresses. These stresses are formulated using a Boussinesq-based eddy viscosity model: A Smagorinsky-type model is used to formulate the eddy viscosity. A dynamic Lagrangian procedure, formulated by Meneveau et al.[9] is invoked to parameterize the subgrid scale stresses. The equations are integrated in time using the fractional step method [10]. In the current solution procedure, the convective terms are represented using an explicit Adams-Bashforth scheme; while the diffusive terms are modeled with an implicit Crank-Nicolson procedure. The spatial derivatives have been discretized with a second-order accurate central difference scheme on a collocated finite-difference stencil. Further details regarding the solver and immersed boundary methodology can be found in [Bozkurttas et al.[2], 2005]. In the current work, we concentrate on simulating flow past deformable fish fins and the method integrated recently to handle this kind of flow problems.

Figure 3. Designation of various nodes on the grid for membranous immersed structure.

The basic concept of the current immersed boundary method is to compute the flow variables for the ghost-cells (*GC*), such that boundary conditions on the immersed boundary in the vicinity of the ghost-cells are satisfied while preserving second-order accuracy. Ghost-cells are those cells whose centers lie inside (or on the other side of) the immersed body and have at least one neighboring cell which lies outside (or on the opposite side of) the immersed body. The process begins by developing the immersed boundary comprised of a number of closely spaced marker points (or elements in 3D) connected by linear segments as shown in Fig. 3 that represents the boundary of the immersed geometry. A non-conformal Cartesian grid is then generated followed by a procedure that identifies the ghost cells. For a membranous structure, two sets of ghost-cells are generated. The schematic in Fig. 3 describes the ghost-cell location scheme.

Following the identification of the ghost cell a probe is extended from the ghost-cells to the immersed boundary such that it intersects normal to the immersed boundary. The intersection of the probe on the immersed boundary is called the boundary intercept point (*BI*). The boundary intercept point is the location where the boundary conditions will be satisfied. Next, the probe extends further into the fluid to a distance equal to the distance between the ghost-cell and the boundary intercept point. The location at the end of the probe is referred to as the image point (*IP*). Four cell nodes that surround the image point are then identified and a bilinear interpolation

$$\phi_{IP} = \sum \beta_i \phi_i \qquad (2)$$

is employed to calculate a value (ϕ) at the image point, where i extends over all the surrounding nodal points and β_i's are the interpolated weights corresponding to the nodes surrounding the image point. All of the information regarding the local geometry of boundary and its placement relative to the mesh is incorporated into these weights (β_i). The flow variables at the ghost-cell are then computed using the value from the image point and boundary-intercept point which line on the normal probe via a second-order interpolation.

III.   Hydrodynamic Performance and Vortex Structures of a Pectoral Fin

Hydrodynamic performance of the bluegill's pectoral fin is examined by carrying out a set of simulations using experimentally observed kinematics. In these simulations, the Strouhal number (defined as St = $L_S f / U_\infty$ where L_S, f and U_∞ are the spanwise size of the fin, fin flapping frequency and fish forward velocity respectively) is 0.54
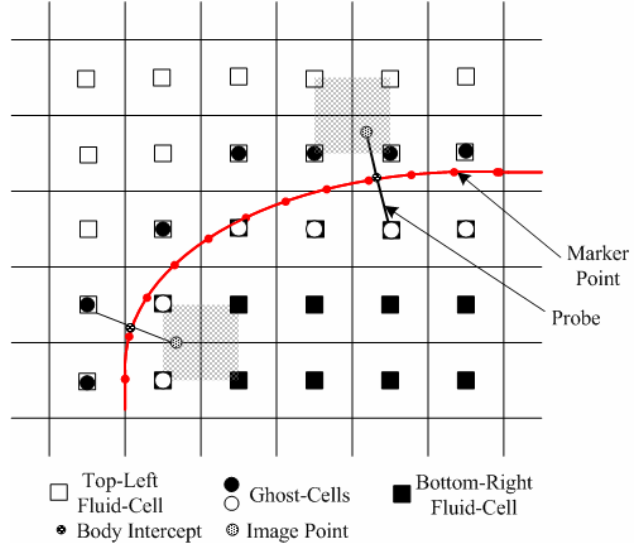
American Institute of Aeronautics and Astronautics, AIAA-2006-1392

and matches that in the experiment. The Reynolds number (defined as $Re_\infty = U_\infty L_S / \nu$) is set to 1440, which is about one-fourth of that in the experiment. Simulations at the experimental Reynolds number are currently being carried out on a finer mesh.

The nominal grid size employed in the current simulations is $153 \times 161 \times 93$ which is about 2.29 million grid points. Comprehensive studies have been carried out to assess the effect of the grid resolution and domain size on the salient features of the flow and also to demonstrate the accuracy of nominal grid size. Figure 4 show the comparisons of time variation of the force coefficients for three different grids. They clearly demonstrate that the hydrodynamic forces computed in the current study are grid and domain independent. Table 1 shows of the mean values of the hydrodynamic force coefficients produced by the fin over one flapping cycle where the coefficient C_F for a given force F is computed as $C_F = F / (1/2) \rho U_\infty^2 A_{fin}$ where A_{fin} is the nominal fin area.

Table 1. Mean force coefficients for flapping fin

| Mean Thrust Coefficient	Mean Lift Coefficient	Mean Spanwise Force Coefficient
1.29	0.24	0.19

(a) Thrust	(b) Lift	(c) Spanwise
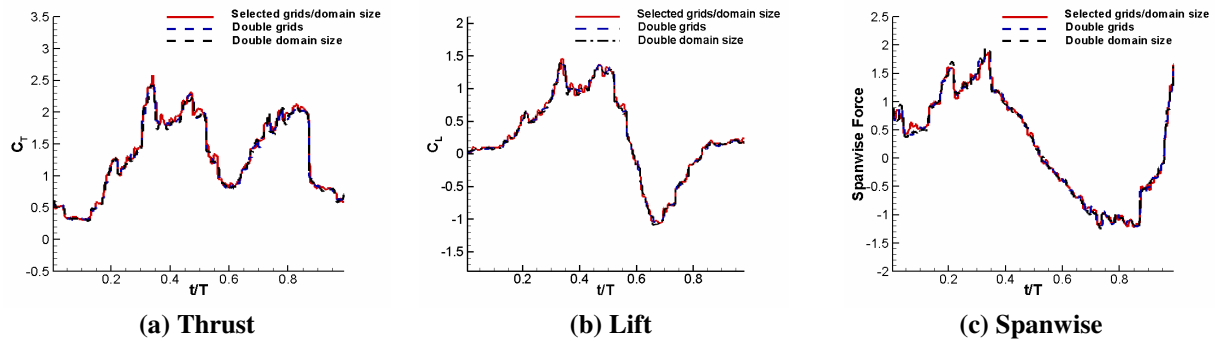
Figure 4. Computed temporal variation of thrust, lift, and spanwise force coefficients for the pectoral fin.

(a) t/T = 1/3	(b) t/T = 2/3	(c) t/T = 1.0
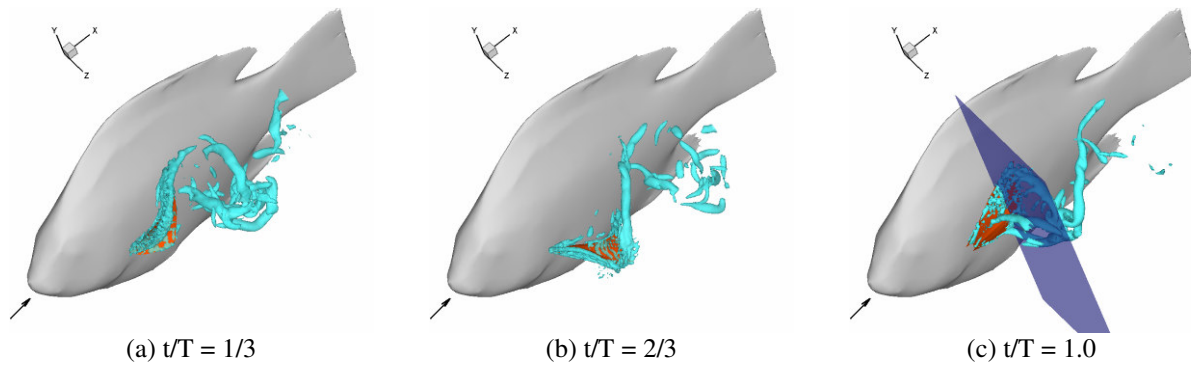
Figure 5. Wake structures for complete motion of fish pectoral fin.

Figure 5(a), (b), (c) show the side view of the vortex structures, the iso-surfaces of the eigenvalue imaginary part of the velocity gradient tensor $\partial u_i / \partial u_j$ [Soria et al.[11], 1993], for the pectoral fin at three different times during one complete cycle of motion, where x and z are the streamwise and spanwise directions respectively. The body of the fish is shown for viewing purpose only and is not included in the simulations. The set of three iso-surface plots show a very complex system of vortices being generated by the fin as it moves through a complete cycle. Of particular note is the strong tip vortex observed in Fig. 5(c) as well as a leading edge vortices created by the top edge of the fin both during abduction and adduction. PIV measurements taken of the flow past the fish pectoral fin in steady swimming

American Institute of Aeronautics and Astronautics, AIAA-2006-1392

are used to validate the current simulations. It should be noted that the fish fin kinematics which are employed in the CFD are not measured simultaneously with the PIV measurements. Nevertheless, we expect the numerical simulations to match most of the key topological features of the flow. Figure 6(a), (b), (c) show flow velocity vectors from PIV measurements at a streamwise plane shown in Fig. 5(c) which is located roughly $(2/3)L_S$ downstream from the fin root.

| (a) t/T = 0.15 | (b) t/T = 0.35 | (c) t/T = 0.85 |
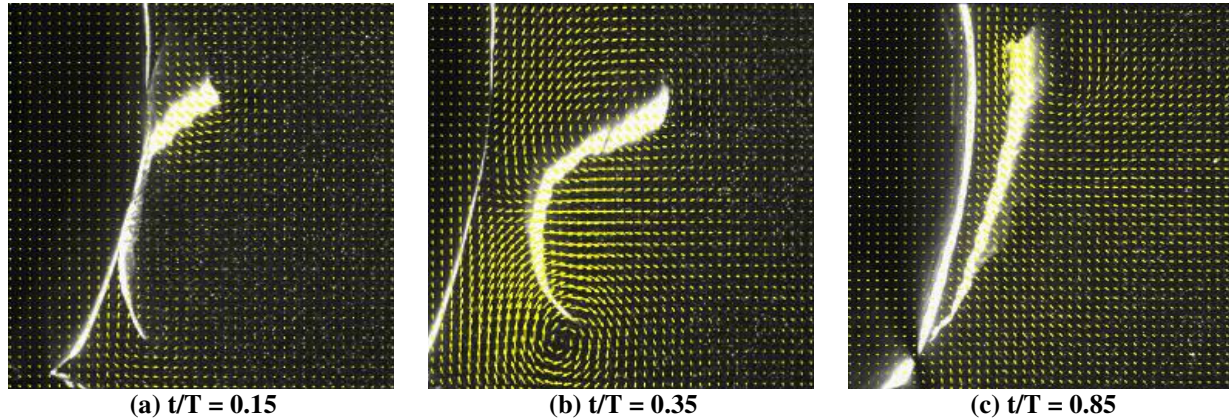
Figure 6. Vector plots on a streamwise plane located at $(2/3)L_S$ from the root of the fin (PIV results).

Figure 6(a) corresponds to an early time in the cycle where the fin is initiating its motion away from the body and is simultaneously undergoing a "cupping" motion that rapidly accelerates its upper and lower fin tips as shown in Fig. 1. A consequence of this rapid acceleration is the formation of two tip vortices where the one at the top is stronger than the one at the bottom. Figure 6(b) is roughly at the 1/3 rd of the cycle and at this time instant CFD and PIV show the presence of two tip vortices. Finally, Fig. 6(c) shows the time instant where the cycle is almost complete and the fin is moving back to the body. At this instant, the PIV measurements show only one vortex which is attached to the upper tip and the CFD simulations also reproduce a similar behavior. Overall, the comparison between the experiments and CFD is quite reasonable and improves our confidence level in the fidelity of the numerical simulations.

One key quantity that the CFD simulations can provide is the hydrodynamic force that is produced by the fin. Figure 4(a) shows the thrust coefficient and it can be observed that not only there are two large peaks of thrust during the full cycle, but that positive thrust is produced during all phases of the cycle. This behavior is very different from behavior exhibited by canonical rigid flapping foils where drag is usually produced at some phases in the cycle [Mittal et al.[12], 2003]. This finding hints at the superior thrust generation capability of this highly deformable fin. The mean thrust coefficient for this case is found to be 1.29. Figures 4(b) and (c) show the other two components of the forces produced by the fin and a number of interesting observations can be made regarding these plots. First, peak magnitudes of these transverse force components are smaller than the peak thrust. This is also highly unexpected since all existing data on rigid flapping foils [Mittal et al.[12], 2003, Lewin et al.[13], 2003, Isogai et al.[14], 1999, Triantafyllou et al.[15], 2004, Dong et al.[16]] shows that the peak thrust is significantly smaller than the peak lift and or spanwise force. This is a clear indication of what we expect to be a relative high propulsive efficiency for this fin. Second, both these forces have positive and negative variations in a cycle that of similar magnitudes. Consequently the mean values of these force components over one cycle are small, 0.24 for lift coefficient and 0.19 for the spanwise force coefficient. These low mean values are not altogether unexpected since they allow the fish to minimize transverse body oscillations as it propels itself forward in a steady manner. Nevertheless, the fact that the current simulations are able to predict this behavior provides further proof of the fidelity of the extracted fin kinematics and the computational modeling approach.

IV. Proper Orthogonal Decomposition of the Pectoral Fin Kinematics and Associated Hydrodynamics

The kinematics of the pectoral fin and the resulting hydrodynamics is highly complex and does not lend itself easily to analysis based on simple notions of pitching/heaving/paddling kinematics or lift/drag based propulsive mechanisms. A more inventive approach is therefore needed which will allow us to dissect this highly complex motion and gain insight into the remarkable hydrodynamic performance of this pectoral fin. Proper Orthogonal
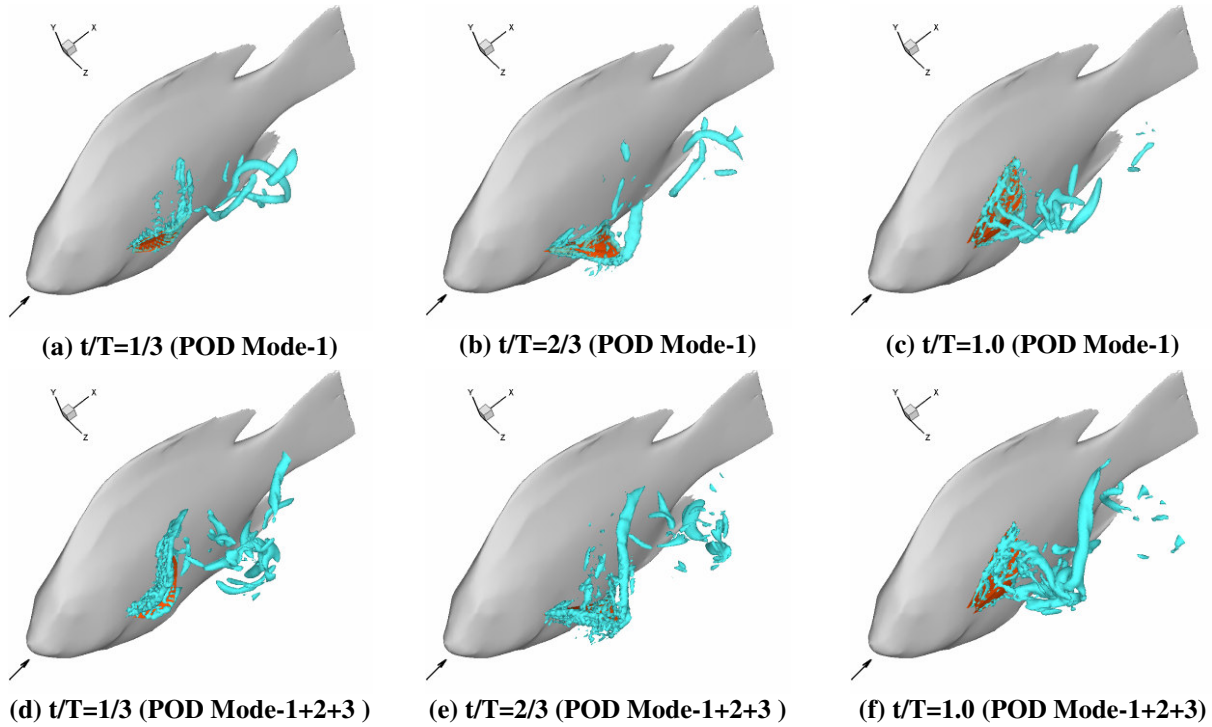
Decomposition is used to extract the essential features of the bluegill's fin kinematics. POD is a powerful and elegant method for data analysis aimed at obtaining low-dimensional approximate descriptions of a high-dimensional process or dataset [Liang et al.[17], 2002]. The POD method has been used in many disciplines including random variables, image processing, data reduction [Barber et al.[18], 2005] and turbulent flow analysis, but our use of this technique for studying fish fins represents a first-of-its-kind effort. The most striking feature of the POD is its optimality: it provides the most efficient way of capturing the dominant components of an infinite-dimensional process with only a finite number of "modes", and often surprisingly few "modes" [Liang et al.[17], 2002]. The POD approach consists of three methods; the Karhunen-Loève Decomposition (KLD), the principal component analysis (PCA), and the singular value decomposition (SVD) which is the one employed in this study.

In the current POD analysis of the fin kinematics, we use 20 distinct time-frames that cover the full cycle of pectoral fin motion. The surfaces at every time frame of the cycle are extracted by using stereo light video and defined by triangular elements. The displacements taken by every node on the pectoral fin surface at each of these time-frames are inserted into a matrix. The matrix is subjected to SVD which then leads to 19 POD modes. Figure 7 shows the singular value spectrum for the fin kinematics. The singular values are normalized by the sum of all the singular values whereas the cumulative values are rescales so that they sum to unity. The singular value spectrum shows three distinct ranges: the first between Mode-1 and 5 where we see a rapid decrease in the amplitude, the second from Mode-5 to 11 where there is a much slower reduction in amplitude and finally the range from Mode-12 to 19 which contains negligible energy. The rapid initial decrease in the spectrum is interesting in that it suggests that a small number of modes contain most of the essential features of the fin gait. In fact, the cumulative values show that the first two, three and five modes capture 55%, 67% and 80% of the total motion respectively. In the current study we are focusing on the first three modes because firstly they capture close to two-third of the total motion and secondly because each of these modes is highly distinct and relatively easy to interpret. Mode-1 is a "cupping" motion where the fin cups forward as it is abducted and leads to a rapid acceleration of the fin leading and trailing edges. Mode-2 is an "expansion" mode where the fin expands to present a larger surface area during adduction and Mode-3 involves a spanwise "flick" of the dorsal edge of the fin.

POD analysis is taken a step further by performing simulations of fin gaits synthesized from the POD modes. This approach has the potential of allowing us to connect specific features in the fin gait with the observed vortex dynamics and hydrodynamics force production. The fin gaits have been synthesized by considering Mode-1, Mode-1+2 and Mode-1+2+3. The POD-synthesized gaits simulations are carried out on the same grid and at the same Reynolds and Strouhal numbers as the complete fin motion simulations for which vortex structures are presented in Fig. 5(a), (b) and (c). In Figure 8, the iso-surfaces of the eigenvalue imaginary part of the velocity gradient tensor are plotted in to show the vortex topology for POD synthesized fin gaits. In this figure (a), (b) and (c) show Mode-1 case at three different time steps and (d), (e) and (f) present Mode-1+2+3 gait simulation at the same time steps. We observe that the tip vortices produced in Mode-1 case are not as strong as the complete fin motion. Furthermore, Mode-1 simulation shows the formation of a distinct vortex ring in the fin wake which is not readily apparent for the fin when it undergoes the complete motion. However, including first three most energetic modes, the observed vortex topology is similar to that of the complete motion with comparable strong tip vortices (see Figure 5(c) & 8(f)).
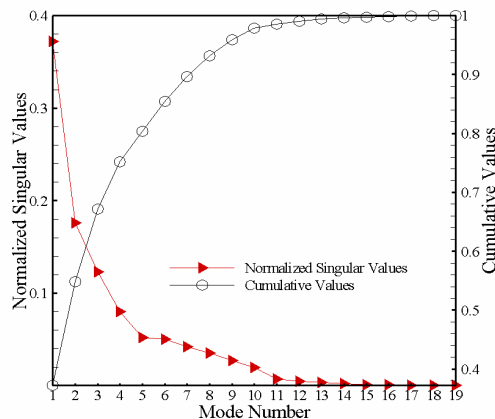

**Figure 7. Normalized singular and cumulative values
extracted from POD analysis of fin motion.**

American Institute of Aeronautics and Astronautics, AIAA-2006-1392

(a) t/T=1/3 (POD Mode-1)   **(b) t/T=2/3 (POD Mode-1)**   **(c) t/T=1.0 (POD Mode-1)**

(d) t/T=1/3 (POD Mode-1+2+3)   **(e) t/T=2/3 (POD Mode-1+2+3)**   **(f) t/T=1.0 (POD Mode-1+2+3)**

Figure 8. Wake structures for POD Mode-1 and POD Mode-1+2+3 of fish pectoral fin.

Figure 9 shows the comparison of time variations of thrust coefficient C_T . It is observed that all synthesized gait cases are thrust-producing during the full cycle of the motion as in the complete motion. In Mode-1, the "cupping" motion captures the first peak of thrust coefficient with a smaller amplitude. The second peak is almost non-existent in this mode. With "expansion" (Mode-2) added to Mode-1, thrust production is enhanced to some extent during the first part of the cycle. However, the second peak of the complete motion is better captured and produces a higher amount of thrust than the Mode-1 case. In Mode-1+2+3 gait, thrust improves remarkably and matches well with the complete motion until ¾'s of the cycle, whereas during the last quarter of the cycle it is just slightly higher than the Mode-1+2 case. It can be concluded that this part of the thrust production, basically the second peak of the complete

motion observed close to the end of the cycle is due to the remaining energetic modes. Fin gait synthesized from Mode-1+2+3+4+5 will be simulated later as well. Table 2 summarizes the hydrodynamics performance results of all the simulations that have been carried so far. It is worthwhile to point out that Mode-1 contains 37% of the total motion (as measured by the magnitude of the singular value), whereas it produces 45% of the total thrust. Similar tendencies are also observed for the other synthesized gaits, where Mode-1+2 represents 55% of the motion, it produces 63% thrust. Mode-1+2+3 corresponds to 67% of the total motion and the thrust production with this gait is 92%. As it is seen, synthesized gait with the inclusion of first three most energetic modes is sufficient to produce most of the thrust and this is important from the point of view of flow physics as well as in the construction of motion schemes for an engineered fin. It is also essential to note that Mode-1 is the most efficient gait with a 75% value.
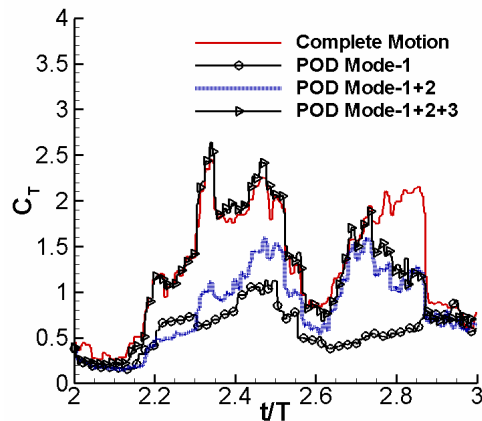
Figure 9. Comparison of thrust coefficient between complete motion and POD synthesized gaits.

American Institute of Aeronautics and Astronautics, AIAA-2006-1392

Table 2.   Comparison of hydrodynamic performance between complete motion and POD synthesized fin gaits

	Thrust Coefficient	Efficiency (%)	Motion (%)	Thrust Production (%)
Complete Motion	1.29	52.3	100	100
POD Mode-1	0.58	74.7	37	45
POD Mode-1+2	0.81	57.5	55	63
POD Mode-1+2+3	1.19	50.0	67	92

V.   Flow past two-dimensional flapping foils with active chordwise deformation

A complimentary approach to POD analysis for determining an effective fin gait for the AUV propulsor is to study a 2D flapping foil with a limited degree of deformation (see Fig. 2) and examine what type of active deformation can improve performance over a comparable rigid foil [Bozkurttas et al.[19],2005]. The prototypical fin that is designed for the potential AUV consists of a flexible membrane stretched across a framework of a small number (<10) rays each of which can be rotated about their roots independently. A CAD model of the fish fin-like propulsor with four rays designed by Ian Hunter's Group at MIT is shown in Fig. 10 [Lauder et al.[20], 2005]. The rays provide a means for actively deforming the chord of the fin during its flapping motion and the issue then is to understand the hydrodynamic performance of such a flapping fin. The central ray is assumed to heave sinusoidally with its displacement given by;

$$h(t) = h_1 \sin\left(2\pi f t\right)$$

where h_1 is the heave amplitude and f is the frequency. In addition we specify the temporal variation of the pitch angles (α) for each segment of the deformable foil (in this case there are two segments) as;

$$\alpha^{(n)}(t) = A^{(n)} \sin\left(2\pi f t + \varphi^{(n)}\right)$$

where "n" corresponds to the segment number, A is the pitch amplitude and φ is the phase difference between pitch and heave motion. In addition to $A^{(n)}$ and $\varphi^{(n)}$, the other non-dimensional parameters that govern the fluid dynamics of this configuration are the normalized heave amplitude $h_1^* = h_1/c$ (where c is the foil chord), the Reynolds number $Re_\infty = U_\infty c/\upsilon$ and the Strouhal number $St = 2fh_1/U_\infty$ based on the wake width. In addition, the location of the central hinge is also a free parameter and is defined in terms of $x_h^* = x_h/c$ where x_h is the distance of the hinge from the leading edge of the foil.
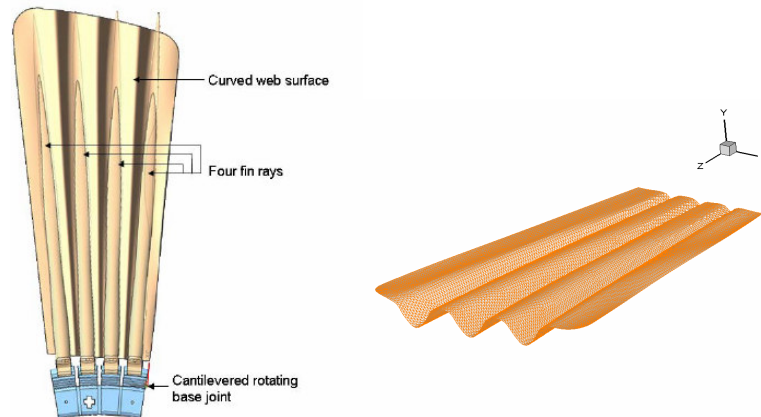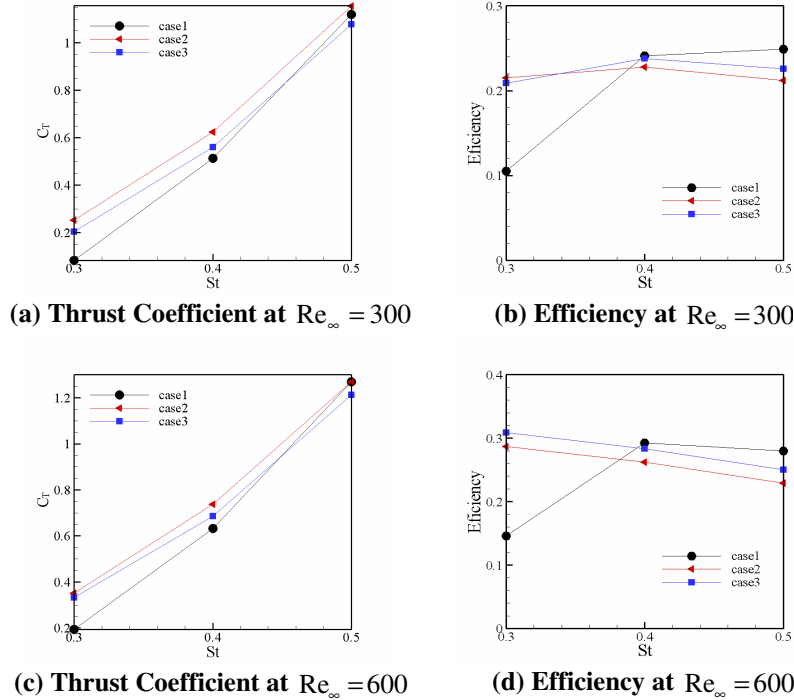

Figure 10. Prototypical of fish fin-like propulsor [Lauder et al.[20], 2005]

Thus, even this rudimentary fin with three rays there are eight non-dimensional parameters. Since we are interested in thrust production, we assume $\varphi^{(1)} = \varphi^{(2)} = \pi / 4$. Furthermore we fix the following values: $h_1^* = 0.5$, $A^{(1)} = 30^\circ$ and $\mathrm{Re}_\infty = 300$ and examine the effect of $A^{(2)}$, x_h^* and Strouhal number on the performance of the foil. A 321×193 Cartesian grid is used in the current simulations within the domain size of 10 x 20. The foil is 6 % thick rounded edge flat plate with a chord length of 1.0. Although a large number of simulations have been carried out, we presented of three selected simulations that highlight the potential benefits of active chordwise deformation. Table 3 shows the kinematic parameters for these three cases where it should be noted that the first case essentially amounts to a baseline rigid flapping foil. The Strouhal numbers for all these cases are varied from 0.3 to 0.5. The same cases are repeated at a Reynolds number of 600.

**Table 3.   Kinematics parameters of simulations**

Cases	$A^{(2)}$	x_h^*	Remarks
Case-1	30	-	Rigid
Case-2	15	0.25	Hinge near LE
Case-3	15	0.50	Hinge at Center

(a) Thrust Coefficient at $\mathrm{Re}_\infty = 300$ **(b) Efficiency at** $\mathrm{Re}_\infty = 300$

(c) Thrust Coefficient at $\mathrm{Re}_\infty = 600$ **(d) Efficiency at** $\mathrm{Re}_\infty = 600$

Figure 11. Effect of Strouhal number and Reynolds number on hydrodynamic performance of actively deformable flapping foils.

Figure 12 presents the spanwise vorticity contours at $\mathrm{Re}_\infty = 300$ for Case-1 and Case-2 at one instant in the cycle for $\mathrm{St} = 0.3, 0.5$. Figure 11 shows the variation of thrust coefficient and propulsive efficiency with Strouhal number for these three cases at two different Reynolds numbers. For both Reynolds number, it is found that in general the performance of the three foils is similar at the higher Strouhal numbers. This is to be expected since at higher Strouhal number the effective angle-of-attack of the body becomes quite large and the leading edge vortex formation process becomes less sensitive to the foil shape. At lower Strouhal numbers such as 0.3, the deformable foils exhibit better performance than the corresponding rigid foil. In particular we observe that both the thrust and the efficiency of the deformable foils are higher than the rigid foil. Also worth pointing out is the fact that the deformable foils have

American Institute of Aeronautics and Astronautics, AIAA-2006-1392

a much flatter variation of propulsive efficiency than the rigid foils indicating that active deformation might allow fish to propel themselves efficiently over a wide operational envelope.

(a) Case-1, $St = 0.3$ (b) Case-2, $St = 0.3$

(c) Case-1, $St = 0.5$ (d) Case-2, $St = 0.5$
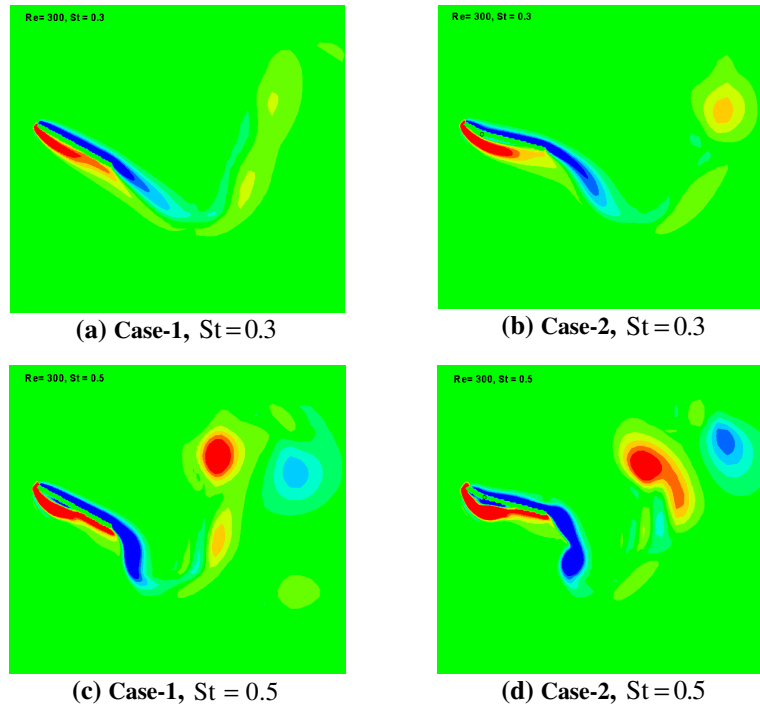
Figure 12. Spanwise vorticity contours for Case-1 and Case-2 at
$\text{Re}_\infty = 300$

References

[1]Drucker, E. and Lauder, V., "Experimental hydrodynamics of fish locomotion: functional insights from wake visualization," *Integ. and Comp. Biol.*, Vol. 42, 2002, pp. 243-257.

[2]Bozkurttas, M., Dong H., Seshadri V., Mittal R., Najjar F. "Towards numerical simulation of flapping foils on fixed Cartesian grids," *AIAA 2005-0079*, Reno, NV, 2005.

[3]Koochesfahani, M.M., "Vortical patterns in the wake of an oscillating airfoil," *AIAA Journal,* Vol.27, Sep. 1989, pp. 1200-1205.

[4]Anderson, J.M., *Vorticity control for efficient propulsion*, PhD Thesis, Massachusetts Institute of Technology, 1996.

[5] Mittal, R., "Computational modeling in bio-hydrodynamics: trends, challenges and Recent Advances," *IEEE J. Oceanic Engineering*, Vol. 29, No: 3, pp. 595-604, 2004.

[6]Katz, J., and Weihs, D., "Hydrodynamic propulsion by large amplitude oscillations on an airfoil with chordwise flexibility,"*J. Fluid Mec.,* Vol. 88 , 1978, pp. 485-497.

[7]Prempraneerach P., Hover F.S., Triantafflyou M.S., "The effect of chordwise flexibility on the thrust and efficiency of a flapping foil*," Proceedings of 13th International Symposium on Unmanned Untethered Submersible Technology (UUST)*, 2003.

[8]Ramamurti, R., Sanberg, W.C., Löhner, R., Walker, J.E., Westneat, M.W., "Fluid dynamics of flapping aquatic flight in the bird wrasse: three dimensional unsteady computations with fin deformations," *The Journal of Experimental Biology 205*, 2002, pp. 2297-3008.

[9]Meneveau, C., Lund, T.S., and Cabot, W.H., "A Lagrangian dynamic subgrid-scale model of turbulence," *J. Fluid Mechanics*, Vol. 319, 1996, pp. 353-385.

[10]Chorin, A.J., "A numerical method for solving incompressible viscous flow problems," *J. Comp. Phys.*, Vol. 2, 1967.

[11]Soria, J., and Cantwell, B. J., "Identification and classification of topological structures in free shear flows," Eddy Structure Identification in *Free Turbulent Shear Flows,"* edited by J. P. Bonnet and M. N. Glauser, pp 379-390, 1993.

[12]Mittal, R., Akhtar, I., Bozkurttas, M., and Najjar, F. M., "Towards a conceptual model of a bio-robotic AUV: Pectoral Fin Hydrodynamics," *Proceedings of 13th International Symposium on Unmanned Untethered Submersible Technology (UUST)*, 2003.

[13]Lewin, G.C.& Haj-Hariri, H., "Modeling thrust generation of a low dimensional heaving airfoil in a viscous flow," *J. Fluid Mec.* , 492, 2003, pp. 339-362.

[14]Isogai, K., Shinmoto, Y., Watanabe, Y., "Effects of dynamic stall on propulsive efficiency and thrust of flapping foil," *AIAA J. 37*, No. 10, 1999, pp. 1145-1151.

[15]Triantafyllou, M.S., Techet A.H., and Hover, F. S., "Review of experimental work in biomimetic foils," *IEEE J. Ocean Engineering*, Vol. 29, No. 3, July 2004.

[16]Dong, H., Mittal, R., Bozkurttas, M., and Najjar, F., "Wake structure and performance of finite aspect-ratio flapping foils," *AIAA 2005-0081*, Reno, NV, 2005.

[17]Liang, Y.C., Lee, H.P., Lim, S.P., Lin,W.Z., Lee, K.H., Wu, C.G.,"Proper orthogonal decomposition and its applications-Part I: Theory,", *J. Sound and Vibration,* Vol 252(3), 2002, pp. 527-544.

[18]Barber, T.J., Ahmed, M.H., and Shafi, N.A, "POD snapshot data reduction for periodic flows," *43rd Aerospace Sciences and Meeting Exhibit*, Reno, NV, 2005.

[19]Bozkurttas, M., Dong, H., Mittal, R., Madden, P., Lauder, G., and Najjar, F., "Simulation of flow past flapping foils with active chordwise deformation," *AIAC 2005-034, Ankara International Aerospace Conference*, METU, TURKIYE, 2005.

[20]Lauder G., Madden P., Hunter I., Tangorra J., Davidson N., Proctor L., Mittal R., Dong H., Bozkurttas, M, "Design and performance of a fish fin-like propulsor for AUVs", *Proceedings of 14th International Symposium on Unmanned Untethered Submersible Technology (UUST)*, 2005.